Polarization diversity for millimeter spaceborne doppler radars: An answer for observing deep convection?

Polarization Diversity for Millimeter Spaceborne Doppler Radars: An Answer for Observing Deep Convection?

ALESSANDRO BATTAGLIA

University of Leicester, Leicester, United Kingdom

SIMONE TANELLI

Jet Propulsion Laboratory, California Institute of Technology, Pasadena, California

PAVLOS KOLLIAS

Department of Atmospheric and Oceanic Sciences, McGill University, Montreal, Canada

(Manuscript received 18 April 2013, in final form 9 July 2013)

ABSTRACT

Spaceborne Doppler radars have the potential to provide key missing observations of convective vertical air motions especially over the tropical oceans. Such measurements can improve understanding of the role of tropical convection in vertical energy transport and its interaction with the environment. Several millimeter wavelength Doppler radar concepts have been proposed since the 1990s. The Earth Clouds, Aerosols, and Radiation Explorer (EarthCARE) Cloud Profiling Radar (CPR) will be the first Dopplerized atmospheric radar in space but has not been optimized for Doppler measurements in deep convective clouds.

The key challenge that constrains the CPR performance in convective clouds is the range–Doppler dilemma. Polarization diversity (PD) offers a solution to this constraint by decoupling the coherency (Doppler) requirement from the unambiguous range requirement. Careful modeling of the radar signal depolarization and its impact on radar receiver channel cross talk is needed to accurately assess the performance of the PD approach.

The end-to-end simulator presented in this work allows reproduction of the signal sensed by a Doppler radar equipped with polarization diversity when overpassing realistic three-dimensional convective cells, with all relevant cross-talk sources accounted for. The notional study highlights that multiple scattering is the primary source of cross talk, highly detrimental for millimeter Doppler velocity accuracy. The ambitious scientific requirement of $1\,\mathrm{m\,s^{-1}}$ accuracy at 500-m integration for reflectivities above $-15\,\mathrm{dB}Z$ are within reach for a W-band radar with a 2.5-m antenna with optimal values of the pulse-pair interval between 20 and 30 μs but only once multiple scattering and ghost-contaminated regions are screened out. The identification of such areas is key for Doppler accuracies and can be achieved by employing an interlaced pulse-pair mode that measures the cross and the copolar reflectivities. To mitigate the impact of attenuation and multiple scattering, the Ka band has been considered as either alternative or additional to the W band. However, a Ka system produces worse Doppler performances than a W-band system with the same 2.5-m antenna size. Furthermore, in deep convection it results in similar levels of multiple scattering and therefore it does not increase significantly the depth of penetration. In addition, the larger footprint causes stronger nonuniform beam-filling effects. One advantage of the Ka-band option is the larger Nyquist velocity that tends to reduce the Doppler accuracies. More significant benefits are derived from the Ka band when observing precipitation not as intense as the deep convection is considered here.

This study demonstrates that polarization diversity indeed represents a very promising methodology capable of significantly reducing aliasing and Doppler moment estimate errors, two main error sources for Doppler velocity estimates in deep convective systems and a key step to achieving typical mission requirements for convection-oriented millimeter radar-based spaceborne missions.

1. Introduction

The monitoring and tracking of changes in convective storm systems can provide hints on how our climate is changing (Allan and Soden 2008). However, the lack of

Corresponding author address: Alessandro Battaglia, Department of Physics and Astronomy, University of Leicester, University Road, Leicester LE1 7RH, United Kingdom.
E-mail: ab474@le.ac.uk

DOI: 10.1175/JTECH-D-13-00085.1

basic formulation aspects (closure, entrainment–detrainment, and downdraft) of convective parameterizations (Yano et al. 2013) significantly hampers the ability of global and regional models to simulate long-term precipitation trends. This is clearly highlighted by a number of major model biases, including 1) biases in the convective transport of moisture, momentum, heat, trace gases, and aerosols from the boundary layer to the upper troposphere with too widespread and too weak model transports (Parazoo et al. 2011); 2) misrepresentation of precipitation rates with precipitation far too frequent and too light (Stephens et al. 2010); 3) inability to represent important modes of variability and convective organization (Zhang and Song 2009); 4) errors in the mean locations of convective precipitation and incorrect diurnal timing of the development, propagation, and precipitation of severe convective storms (Trenberth et al. 2003); and 5) inaccuracies in the links between storm dynamics and microphysics (van den Heever and Cotton 2004) with obvious repercussions for cloud radiative forcing, surface precipitation, and vertical heating.

Convective vertical air motion is a key atmospheric parameter that affects cloud microphysics, radiation, and lifetime (Phillips and Donner 2006). Despite its importance, no measurements of vertical air motion are available globally especially over the tropical oceans. Spaceborne Doppler radars have the potential of acquiring global distribution of the vertical motions in clouds and precipitation. Such measurements could provide a better understanding of precipitation processes and dynamics on a global scale (e.g., by measuring vertical profiles of latent heat fluxes) and improve the characterization of convection (vertical profiling and temporal evolution) and GCM's skills by assimilating vertical velocity.

The 94-GHz *CloudSat* radar (Tanelli et al. 2008a) spearheaded the observation of the upper part of convective plumes (e.g., Luo et al. 2008; Bacmeister and Stephens 2011; Luo and Stephens 2010). However, *CloudSat* has no Doppler capability and thus no direct characterization of the convective intensity of clouds is possible. The joint European Space Agency (ESA)–Japan Aerospace Exploration Agency (JAXA) Earth Clouds, Aerosols, and Radiation Explorer (EarthCARE) mission is scheduled for launch in 2016 and features the first atmospheric Cloud Profiling Radar (CPR) with Doppler capability in space. Recently, several other spaceborne Doppler radar concepts (Tanelli et al. 2009) have been proposed. Examples include the Polar Precipitation Mission (PPM; Joe et al. 2010) proposed for the ESA Earth Explorer program, the Climate Dynamics Mission (CLDY) proposed as part of the ESA's International Space Station (ISS) Climate Change program, and the National Aeronautics and Space Administration (NASA)'s Aerosol Cloud and Ecosystems Mission (ACE; National Research Council of the National Academies 2007; Durden et al. 2011). The aforementioned proposed concepts aim at targeting the characterization of frozen precipitation over the polar and immediate regions, at improving our understanding of critical convective cloud and precipitation processes, and at quantifying aerosol–cloud interaction and assessing the impact of aerosols on the hydrological cycle.

The typical minimum scientific requirement in convection is to achieve Doppler accuracies better than $1\,\mathrm{m\,s^{-1}}$ at a cloud resolving scale (0.5–2 km). Analysis of *CloudSat* observations indicates that strong attenuation limits the penetration of a 94-GHz spaceborne radar only to the upper part of deep convective clouds. To this end, addition of a Ka-band (i.e., about 35 GHz) channel is expected to penetrate a larger portion of deep convective systems; however, it will also result in a larger beamwidth (2.7 times larger than the W band for the same antenna size).

The larger radar beamwidth at 35 GHz is likely to cause larger velocity biases due to Nonuniform Beam Filling (NUBF; Tanelli et al. 2002a; Schutgens 2008; Kollias et al. 2013, manuscript submitted to *J. Atmos. Oceanic Technol.*). Despite these drawbacks, we consider here the matched antenna solution since it has been accepted as the preferable option by the science teams supporting Ka- and W-radar missions (Bennartz et al. 2011; Tanelli et al. 2009) as opposed to reducing the illuminated portion of the W-band channel, given a maximum allocated size for the physical two frequency antenna. In addition to NUBF, there are three issues that impact the quality of the Doppler velocity measurements from a spaceborne millimeter wavelength radar in convection:

(i) the presence of multiple scattering (MS) that can overwhelm the single scattering (SS) contribution in optically thick media making the interpretation of the signal extremely complex (Battaglia et al. 2010, and references therein);
(ii) velocity folding induced by the low Nyquist velocity in conjunction with the large vertical velocities and extreme wind shear (up to $2 \times 10^{-3}\,\mathrm{s^{-1}}$; Heymsfield et al. 2010) encountered in convective cores; and
(iii) uncertainty in the Doppler velocity estimate introduced by the short coherency time of the signal (down to $60\,\mu\mathrm{s}$) due to the motion of the satellite, the finite beamwidth, and the turbulence (Tanelli et al. 2003; Kollias et al. 2013, manuscript submitted to *J. Atmos. Oceanic Technol.*).

While the first issue has been addressed in Battaglia et al. (2011), who proposed a criterion to identify MS-contaminated areas, innovative millimeter radar concepts must be investigated to overcome the second and the third issues. This paper focuses on assessing the potential offered by polarization diversity (PD; Doviak and Sirmans 1973; Pazmany et al. 1999; Kobayashi et al. 2002, 2003). The implementation of PD in millimeter spaceborne Doppler radars can reduce the Doppler velocity uncertainty by sampling faster the atmosphere and mitigate the velocity folding challenge by increasing the Nyquist velocity.

While section 2 recalls the main drivers of spaceborne Doppler system coherency time and its relationship with the Doppler spectral width, section 3 revisits the PD concept with specific attention paid to describing its pros and cons. An initial assessment of the improved accuracy of a PD radar system compared to the traditional single-polarization method is carried out. More rigorous notional studies for 3D convective scenarios are conducted in section 4. After describing the radar end-to-end simulator with details on the signal processing component tailored to the PD analysis, a convective scenario is used to illustrate the simulator outputs. A statistical analysis is applied to a large dataset of simulated convective profiles to optimize the pulse-pair (PP) interval of the PD system. Summary and conclusions are then presented in section 5.

2. Spectral width and coherency time for spaceborne Doppler radars

We briefly recall that in *uniform beam-filling conditions* the total velocity spectral width σ_D may be estimated by considering the various physical phenomena that cause a spread of Doppler velocities (Kobayashi et al. 2003), that is, wind shear, turbulence, the natural variance in hydrometeor terminal velocity, and Doppler fading due to satellite motion. The total variance of the Doppler spectrum is given by

$$\sigma_D^2 = \sigma_H^2 + \sigma_{\mathrm{vsvw}}^2 + \sigma_{\mathrm{vwT}}^2 + \sigma_{\mathrm{comb}}^2 . \tag{1}$$

The associated time scale of radar decorrelation signal is given by

$$T_{\mathrm{dec}} = \frac{\lambda}{2\sqrt{2}\pi\sigma_D}. \tag{2}$$

In Eq. (1), σ_H is due to the spread of the terminal fall velocities of hydrometeors of different size, σ_{vsvw} is the broadening due to the vertical shear of the vertical wind [linearly proportional to the vertical resolution of the radar; Doviak and Zrnić (1984)], σ_{vwT} is the broadening of the vertical wind due to turbulent motions in the atmosphere [with values ranging from 1 to $4\,\mathrm{m\,s^{-1}}$ for standard and extreme turbulence; Amayenc et al. (1993)], and σ_{comb} is the spread caused by the coupling between the platform motion and the vertical wind shears of the horizontal winds (details in Kobayashi et al. 2002):

$$\sigma_{\mathrm{comb}} = \frac{\theta_{3\mathrm{dB}}}{4\sqrt{\log(2)}}[(-V_{\mathrm{sat}} + \kappa_{\mathrm{zx}}H_{\mathrm{sat}})^2 + (\kappa_{\mathrm{zy}}H_{\mathrm{sat}})^2]^{1/2}, \tag{3}$$

where $\theta_{3\mathrm{dB}}$ is the 3-dB beamwidth of the antenna and V_{sat} and H_{sat} are the spacecraft velocity and altitude, respectively, while K_{zx} and K_{zy} are the horizontal shears of the vertical wind. For a Gaussian circular antenna pattern, and only in case of very weak vertical wind shears, Eq. (3) reduces to (Tanelli et al. 2002a)

$$\sigma_{V_{\mathrm{sat}}} = \frac{\theta_{3\mathrm{dB}}V_{\mathrm{sat}}}{4\sqrt{\log(2)}}. \tag{4}$$

In convection wind shears, values of $5 \times 10^{-3}\,\mathrm{s^{-1}}$ can be observed, which forces to retain Eq. (3).

When dealing with uncertainties in Doppler velocities it is useful (Tanelli et al. 2002b) to introduce a normalized form with the normalizing factor given by twice the Nyquist velocity, $v_{\mathrm{Nyq}} \equiv \lambda \times \mathrm{PRF}/4$ (with λ being the wavelength and PRF the pulse repetition frequency), that is

$$\sigma_N = \frac{2\sigma_D}{\lambda \times \mathrm{PRF}} = \sqrt{\frac{\sigma_{\mathrm{vwT}}^2 + \sigma_{\mathrm{comb}}^2}{4v_{\mathrm{Nyq}}^2}}, \tag{5}$$

where we have further assumed that for low Earth orbit spaceborne configurations the first two terms in the right-hand side of Eq. (1) are typically negligible. Accuracy in Doppler estimates may be expressed as (Zrnić 1979; Tanelli et al. 2008b)

$$\mathrm{var}(\langle \hat{v}_z \rangle) = f(\sigma_N, \mathrm{SNR}, v_{\mathrm{zN}})/M^{1/2}, \tag{6}$$

where v_{zN} is the normalized mean Doppler velocity, SNR is the signal-to-noise ratio, M is the number of pulses, and f is a continuous function that increases monotonically with σ_N and decreases asymptotically with SNR.

The second term in the square root of Eq. (5) is inversely proportional to the square of the antenna diameter D ($\theta_{3\mathrm{dB}} \propto \lambda/D$ for circular antennas). When this term is the dominant one, W and Ka radars with the same antenna size produce the same σ_N and T_{dec}. Considering

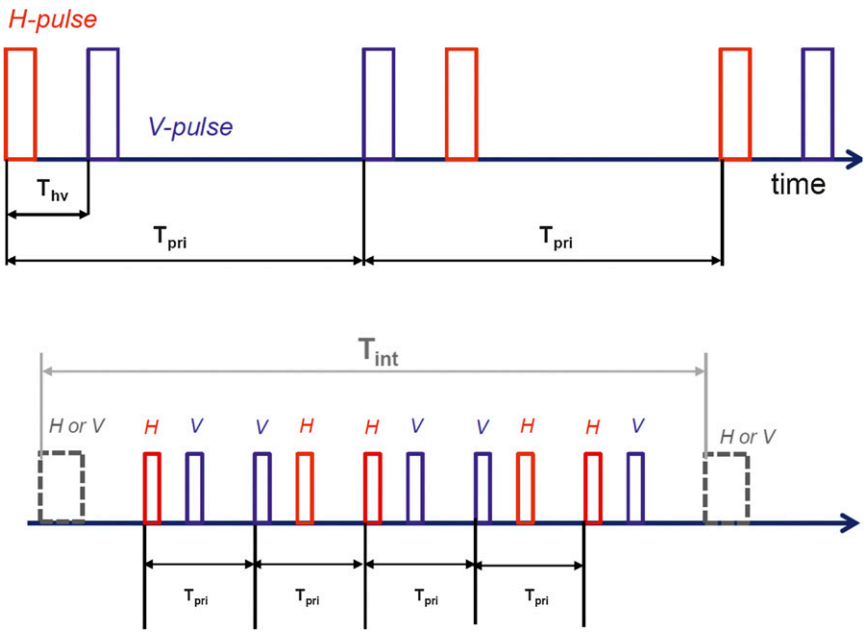

FIG. 1. (top) Pulse patterns of orthopolarization diversity. The terms H and V denote polarimetries in the H and V directions, respectively; while T_{hv} and T_{pri} represent a pulse-pair interval and a pair repetition interval, respectively. In this example, one vh and two hv pairs are shown. (bottom) Schematic for the interlaced PP and PDPP mode. The T_{int} is the repetition interval of the interlaced mode, typically $T_{int} \gg T_{pri}$.

Eq. (6), Ka systems are favored by larger SNR deep into the convective cores (thanks to less attenuation) and by smaller v_{zN} thanks to larger v_{Nyq}, but they have lower *SNR* in the upper part of the convection (because of lower sensitivity). The relative significance of the third and fourth term in the right-hand side of Eq. (1) depends on the antenna size and the turbulence magnitude. However, as already noted in Tanelli et al. (2008b), with the same antenna size, the turbulent term tends to create broader normalized spectra for smaller wavelengths. This seems to favor Ka compared to W when looking at convective regions with strong turbulence.

Until now the whole reasoning has been based on the ideal assumption of uniform beam-filling conditions. In NUBF *conditions*, which are very likely to occur for convective clouds and typical footprint sizes, the situation is completely different. In the term σ_{comb} the contribution of the satellite velocity can be completely different from that predicted by Eq. (3), and it can be either larger (e.g., when two highly reflective cells much smaller than the footprint are present at opposite sides along the satellite movement within the radar footprint) or smaller (e.g., when a single highly reflective cell is present within the radar footprint). Because of the typically larger footprints this effect will be of greater relevance at the Ka band. This will add up to the bias already introduced by NUBF (see Tanelli et al. 2002a). Only a fully 3D simulation framework can assess the entity of such an effect.

3. Polarization diversity

The idea of PD for Doppler velocity measurements was first introduced by Doviak and Sirmans (1973) to overcome the range overlap of echoes from a copolar multipulse repetition frequency (PRF) pulse transmission scheme. The PD concept is illustrated in Fig. 1. A radar with polarization diversity measures the first two Doppler moments by simultaneously using two channels to receive the scattered power from two orthogonally polarized pulses, closely spaced with the pulse-pair separation denoted as T_{hv}. Pairs are transmitted separated by the interval (T_{pri}). Despite the use of separate receiver channels for the H and V pulses, their phase coherency (due to the short interval between the H and V transmission) is the key feature to extract the Doppler velocity. In practice, the PD technique effectively decouples the maximum unambiguous range, $r_{max} = cT_{pri}/2$, and the Nyquist velocity, $v_{Nyq} = \lambda T_{hv}/4$, c being the speed of light and λ the radar wavelength.

Pazmany et al. (1999) applied the PD technique to a high-resolution 95-GHz ground-based radar to study the reflectivity and velocity structure in severe thunderstorms, while Kobayashi et al. (2002) proposed it for

spaceborne applications in a nadir-looking configuration and Kobayashi et al. (2003) studied the accuracy in Doppler velocity estimates as a function of the pulse-pair interval T_{hv}. Their study is, however, limited to moderate spectral widths only (i.e., $\sigma_v = 3.85\,\mathrm{m\,s^{-1}}$).

The implementation of a PD scheme in a spaceborne Doppler radar includes several technological challenges including more complex transmit scheme and receiver signal processing. While these challenges can be overcome, it is important to acknowledge that the success of the PD scheme is based on our ability to limit the coupling (cross talk) between the polarizations both at the hardware level and while the wave propagates and scatters. This paper will be mainly devoted to study this aspect.

a. Cross talk

The voltages measured in the two receiving channels that correspond to scattering from range r at time t can be written as

$$V_V(r,t) = V_{vv}(r,t) + V_{vh}(r + \Delta r, t) + N_v(r,t), \quad (7)$$

$$V_H(r,t) = V_{hh}(r,t) + V_{hv}(r - \Delta r, t) + N_h(r,t), \quad (8)$$

where V_{ij} is the signal component of the voltage at the output of the i-polarized receiver when j polarization was transmitted, and N_v and N_h represent system noise in the vertical and horizontal receiver channels, respectively. In this paper we discuss linear polarization. The signal components are a function of the target scattering matrix corresponding to the range cell located at a distance r from the radar at time t of the normalized propagation distortion matrix (which accounts for differential attenuation and phase shift) and of the normalized complex receiver/transmitter distortion matrix (Pazmany et al. 1999). The second terms on the right-hand side of Eqs. (7) and (8) represent cross talk between the receiving channels originated from cells located at ranges $r \pm \Delta r$, with $\Delta r = cT_{hv}/2$, which can affect Doppler velocity estimation by producing a blind zone (neatly explained with a bounce diagram in Fig. 7 in Kobayashi et al. 2002) that reduces the volume where velocity retrievals are meaningful.

The LDR is the ratio between the energy backscattered in the polarization orthogonal to the incident one and the energy backscattered in the same polarization as the incident one. In general, the LDR value is determined by the contributions of three types of propagation cross talk between two orthogonal polarizations and by the instrument internal sources of cross talk:

(i) *Multiple scattering* is a key source of depolarization for spaceborne millimeter radars. This is well know from lidar (e.g., Hu et al. 2001), but it has also been demonstrated that for W-band radars (Battaglia et al. 2007) where the LDR can reach values close to 0 dB when the multiple scattered signal dominates.

(ii) *Depolarizing atmospheric targets:* while spherical particles do not depolarize radiation, nonspherical particles tend to depolarize the radar signal. In general irregular shape tend to enhance the LDR, which generally depends on the hydrometeor microphysical characteristics [size, shape, orientation relative to local vertical direction, phase (liquid, ice, and mixed phase), and particle density (e.g., aggregate or rimed)]. Airborne observations (see Fig. 6 in Wolde and Vali 2001) for near-nadir angles typically show:

- for ice crystal values up to −14 dB for plate–stellar–dendrite (columnar) crystals;
- for melting particles values between −15 and −8 dB; and
- values lower than −22 dB for graupel, drizzle, hexagonal–stellar plates, and dendrites.

(iii) *Ground clutter* tends to depolarize radiation, but this problem is more acute when scanning configurations are considered and over certain land surfaces. Hereafter, a Kirchoff surface in the stationary phase approximation will be considered (Ulaby et al. 1986). Note that in this term we also include bistatic and mirror image contributions (Liao et al. 1999).

(iv) *Instrument cross talk* introduced by different components of the radar hardware (e.g., antenna and orthomode transducer), which contribute to a reduction of the isolation between the two channels. Radars designed for dual-polarization applications typically aim for cross-polar isolation better than −20 dB with −30 dB being a reasonable target.

The LDR characteristics apply to both Ka and W bands.

b. Doppler moments estimators

The conventional PP technique (Doviak and Sirmans 1973) estimates the first two moments of the Doppler spectrum from the autocorrelation function of the radar signal measured both at time zero and at lag $\tau = T_{pri}$. In a noncontiguous pair approach, the two pulses representing a pair are separated by an interval T_1, while two pairs are separated by a longer interval T_2 [i.e., similar to the staggered PRT approach (Sachidananda and Zrnić 2002) but calculating correlation only between the two pulses of the "short pair"]. However, the low limit of T_1 is determined by the same range ambiguity constraints that limit the choice of T_{pri} in the conventional PP. The polarization diversity pulse-pair (PDPP) technique is

basically a noncontiguous pair configuration where such constraint on T_1 is relieved by the fact that the two pulses are transmitted on orthogonal polarizations. In PDPP the autocorrelation function is replaced by the cross-correlation function of the orthogonally polarized signals at lag $\tau = T_{\rm hv}$, defined as (Doviak and Sirmans 1973; Pazmany et al. 1999)

$$\hat{R}_{\rm HV}(r, T_{\rm hv}) = \frac{1}{M}\sum_{i=1}^{M} V_H^*(r, t_i) V_V(r, t_i + T_{\rm hv}) = \hat{R}_{\rm HV}(r, 0) e^{j[2\pi f_D(r) T_{\rm hv} + \Phi_b] - 2\pi^2 \sigma_f^2(r) T_{\rm hv}^2}, \quad (9)$$

where f_D is the mean Doppler shift, σ_f is the standard deviation of the power spectrum, t_i is the sample time of the ith pair's first sample, and the superscript * represents a complex conjugate. The term M represents $M/2$ independent vh pairs combined with $M/2$ independent hv pairs (Fig. 1). The value Φ_b is a phase bias introduced by the differential phase shift induced by the propagation of the H and V polarization pulses in the atmosphere and by any difference in the transmission lines between the two polarization channels in the radar. Note that when inserting Eqs. (7) and (8) into Eq. (9) the expectation of the estimated cross-correlation function reduces to

$$\hat{R}_{\rm HV}(r, T_{\rm hv}) = \frac{1}{M}\sum_{i=1}^{M} V_{\rm hh}^*(r, t_i) V_{\rm vv}(r, t_i + T_{\rm hv}), \quad (10)$$

because only $V_{\rm hh}(r)$ and $V_{\rm vv}(r)$ are correlated. The terms including cross-polarized signals are not correlated being scattered from cells located at different ranges ($r \pm \Delta r$).

The cross-correlation function $R_{\rm VH}(r, T_{\rm hv})$ has a similar expression but with the phase bias Φ_b having the opposite sign. Thus, we can combine the two cross-correlation functions to estimate the Doppler moments:

$$\hat{v}_D = \frac{\lambda}{4\pi\tau} \arg\sqrt{\hat{R}_{\rm HV}(T_{\rm hv}) \hat{R}_{\rm VH}(T_{\rm hv})}, \quad (11)$$

$$\hat{\sigma}_D = \frac{\lambda}{2\pi\sqrt{2}T_{\rm hv}} \sqrt{\log\left|\frac{\hat{R}_{\rm HV}(T_{\rm hv})}{\hat{R}_{\rm HV}(0)}\right|}. \quad (12)$$

As shown in Pazmany et al. (1999) cross-polarization interference, phase, and thermal noise do not bias the phase of $\hat{R}_{\rm HV}$. They therefore do not bias the estimated mean velocity. Their contributions appear as additive contributions to the noise background in most instances well represented by white noise. In this case they cause a reduction of the SNR that in a PP approach only causes an increase in the standard deviation of the mean Doppler velocity. While the cross-polarized terms [second terms on the right side of Eqs. (7) and (8)] will often appear in general as weaker images of the primary (copolarized) return; since the two orthogonally polarized pulses are not transmitted simultaneously, they can also either appear as ghosts (in regions with no significant copolar backscattering return) or add up to the noise in portions of the profile where the copolar backscattering was generated by weaker clouds (see Fig. 2).

c. Interlaced mode

Receiver channel cross-talk–affected regions can be identified when a polarization diversity mode is interlaced with the usual pulse-pair mode (bottom panel in Fig. 1). The V (or H) mode allows measurement of the cross-polar and the copolar reflectivity signals. This immediately leads to the possibility of estimating the LDR as the ratios of the two, which can be used to flag MS-affected regions (Battaglia et al. 2007). The comparison between the copolar reflectivity and the reflectivities as derived from the V^H and V^V sequences [Eqs. (7)–(8)] is useful for the identification of the ghosts and for regions where Doppler estimates will deteriorate. The penalty paid by the introduction of this interlaced mode is a reduction in the number of samples used for Doppler velocity estimates. However, since only reflectivities are sought after and the Doppler analysis is accurate only at regions with high SNR, the single-pulse mode can be inserted intermittently among the main dual-polarization pulses with a repetition interval $T_{\rm int}$ much larger than $T_{\rm pri}$. This will only slightly reduce the Doppler velocity accuracy.

Note that an interlaced concept was proposed by Kobayashi et al. (2002) as well. However, in that case, the polarization diversity pulses were inserted intermittently among the main single-polarization pulses with the explicit goal of providing a good unaliased estimate of the surface Doppler velocity in order to properly correct for antenna mispointing errors.

d. Accuracy of PDPP versus PP for convective scenarios

Perturbation theory has been successfully used to estimate the uncertainty in Doppler velocity measurements [i.e., to compute the function f in Eq. (6) using a pulse-pair estimator if the pulse-pair interval is significantly shorter than the coherency time, for SNR $>$ 0 dB and for sufficient number of independent pulse-pair samples M (Zrnić 1977; Kobayashi et al. 2002, 2003)]. It will be shown that these conditions are satisfied in observations of convective cores with a spaceborne millimeter radar that employs a PDPP technique when typical science requirements are met.

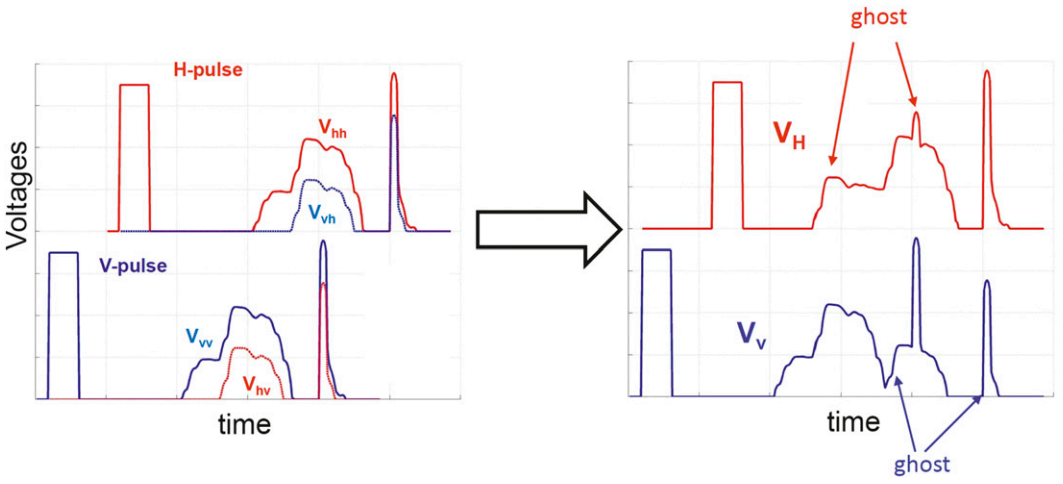

FIG. 2. Illustrating the formation of a "ghost" signal due to cross-talk interference. (left) The V pulse produces both a copolar (V_{vv}) and a cross-polar return (V_{hv}); the same is true for the H pulse. (right) The signal received in the V channel (V_V) is a combination of the copolar return of the V-pulse (V_{vv}) and the cross-polar return of the H pulse (V_{vh}) according to Eq. (7). Similar for the H channel. This may result in reflectivity ghosts as pinpointed by the arrows.

Ground-based radar systems employ the PDPP technique in order to increase the Nyquist velocity and thus mitigate velocity folding. However, this comes at the expense of larger velocity magnitude uncertainty in Doppler velocity estimates [because, with increasing v_{Nyq}, the error in the correlation function phase measurement maps into a larger velocity error; Pazmany et al. (1999)]. In spaceborne Doppler Cloud Profiling Radars (e.g., EarthCARE CPR; Kobayashi et al. 2002), the main advantage of the PDPP technique is the higher sampling of a fast decorrelating signal due to the motion of the satellite. This effectively reduces the normalized spectrum width (which can reach values of about 0.3 for EarthCARE or a Ka system with the same antenna size) and reduces the uncertainty in the Doppler velocity estimates. Thus, for millimeter spaceborne systems, the application of a PDPP scheme is desirable for two reasons:

(i) the expected reduction in the normalized spectrum width (by sampling faster an increasingly incoherent medium due to the satellite motion and the finite beamwidth); and
(ii) the extended Nyquist velocity, with the corresponding reduction of v_{zN} and of the Doppler velocity folding.

The impact of the first factor in the accuracy of Doppler velocity estimates from spaceborne 94-GHz radar system (specifics in Table 1) is shown in the top panel of Fig. 3. Lines correspond to a moderate turbulence scenario (i.e., a turbulence of $3.3\,\mathrm{m\,s^{-1}}$ resulting in a spectral width $\sigma_D = 5\,\mathrm{m\,s^{-1}}$), while the shadowing spans from little/no turbulence (i.e., a turbulence of $1.3\,\mathrm{m\,s^{-1}}$ resulting in a spectral width $\sigma_D = 4\,\mathrm{m\,s^{-1}}$) to strong turbulence (i.e., a turbulence of $4.6\,\mathrm{m\,s^{-1}}$ resulting in a spectral width $\sigma_D = 6\,\mathrm{m\,s^{-1}}$) scenarios. Since the problem is invariant when considering the same normalized velocities and spectral widths (Tanelli et al. 2008b), the same curves amplified by a factor of 2.7 (equal to the ratio of the Nyquist velocities at the Ka and W bands) apply to the Ka system, whose specifics are in Table 1, when considering spectral widths in the range between 10.7 and $16.1\,\mathrm{m\,s^{-1}}$. However, while the broadening due to the finite antenna beamwidth and platform velocity scales with frequency, the turbulence contribution to the broadening does not scale with the frequency, and therefore the Ka-band spectral widths for the same turbulence assumptions are $\sigma_D = 10.4$, 10.8, and $11.3\,\mathrm{m\,s^{-1}}$, respectively, for low, moderate, and strong turbulence. Since 10.8 is 2.7 times 4, the corresponding

TABLE 1. Configuration for W- and Ka-band spaceborne Doppler systems.

Frequency (GHz)	Altitude (km)	Satellite speed ($\mathrm{km\,s^{-1}}$)	θ_{3dB} (°)	$\sigma_{V_{sat}}$ ($\mathrm{m\,s^{-1}}$)	Vertical resolution (m)	PRF (kHz)	Single pulse noise level (dBZ)
94	400	7.6	0.095	3.8	500	7	−21.5
35	400	7.6	0.26	10.3	500	7	−10

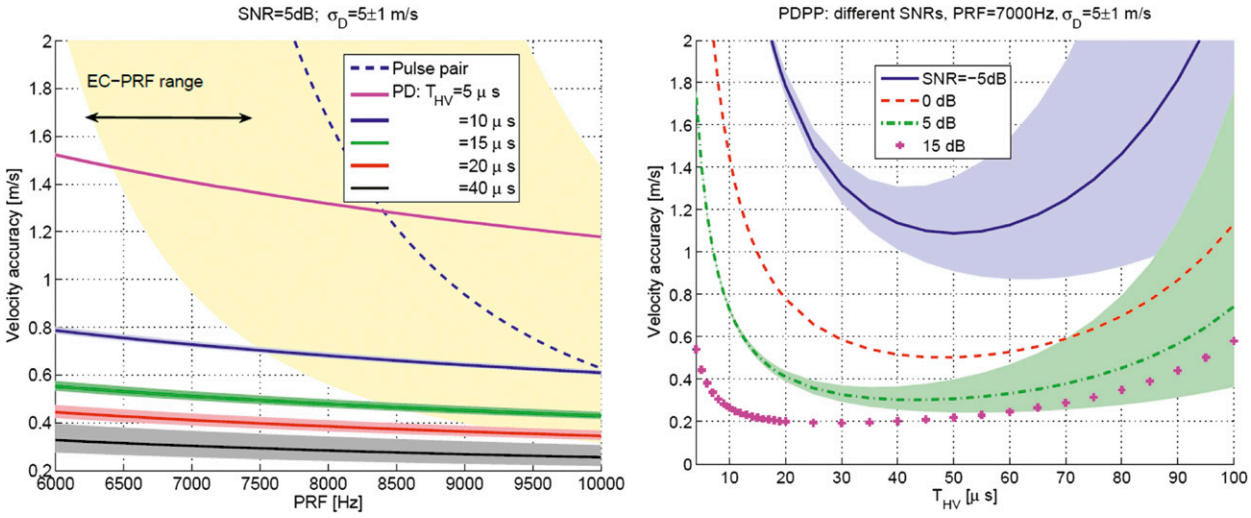

FIG. 3. Velocity accuracy for an EarthCARE CPR–like nadir-pointing configuration (specifics in Table 1) for different (left) PRFs and for different (right) T_{hv}s at PRF = 7 kHz. For the PDPP configuration, T_{pri} is set to be equal to 1/PRF. The integration length is assumed to be 500 m. Lines correspond to spectral widths equal to 5 m s^{-1} while the shadowing spans from little/no turbulence ($\sigma_D = 4$ m s^{-1}) to strong turbulence ($\sigma_D = 6$ m s^{-1}) scenarios. The same curves with the y axis amplified by a factor of 2.7 apply to the Ka system whose specifics are in Table 1 when considering spectral widths in the range between 10.7 and 16.1 m s^{-1}.

normalized spectral width is the same as the low-turbulence case for the W band, and one can use the low-turbulence curve of the W-band configuration in Fig. 3 for the Ka band in all turbulence conditions. Therefore, the SNR and σ_N being equal, the W-band configuration would provide more accurate Doppler estimates than the Ka band. On the other hand, it is also clear that 1) because of the reduced attenuation, the Ka band will likely produce more observations at large SNRs; and 2) because of the already large Doppler fading $\sigma_{V_{sat}}$ (about 10 m s^{-1} for the given antenna; see Table 1), turbulence will not significantly further broaden the spectrum at Ka.

The performances of the single-polarization PP technique (dashed line and yellow shading) are strongly dependent on the PRF and on σ_D because these parameters dictate the pulse-pair distance (ranging between 166 and 100 μs for PRF from 6 to 10 kHz) and the coherency time (ranging from 90 to 60 μs for σ_D from 4 to 6 m s^{-1} at the W band and from 10.7 and 16.1 m s^{-1} at Ka band), respectively. For the low-turbulence scenario ($\sigma_D = 4$ m s^{-1}) the pulse-pair produces reasonably accurate results but with a significant difference when moving the PRF within the EarthCARE CPR range. Instead, in strong turbulence even for PRF = 10 kHz values (which correspond to $v_{Nyq} = 8$ and 21.4 m s^{-1} at the W and Ka bands, respectively, and to $r_{max} = 15$ km thus precluded when observing deep tall convective systems), the velocity accuracy is not achieving the target goal of 1 m s^{-1}. On the other hand for the PD the dependence on the PRF is only marginal, since in that case such a parameter is affecting only the number of samples; vice versa accuracies are strongly dependent on T_{hv}, as already noted by Kobayashi et al. (2002), but are well below 1 m s^{-1} for T_{hv} larger than 10 μs and smaller than 150 μs for positive SNR and 1-km integration.

The bottom panel of Fig. 3 shows the dependence of the PDPP Doppler accuracy as a function of the pulse-pair interval T_{hv} for different SNR values. As already noted by Kobayashi et al. (2002), the accuracy is affected by two competitive effects: 1) the decrease in resolution of the Doppler phase at small T_{hv}s, and 2) the deterioration in correlation at large T_{hv}s. The former effect is more important for lower SNRs, while the latter is more important for higher SNRs and higher σ_Ds (shorter coherency times). This is why the minimum point of each curve shifts from high to low T_{hv} values as the SNRs and/or σ_Ds increase.

As observed in Pazmany et al. (1999) there are different error sources in the measured phase: certainly thermal and phase noise but also the interference between the orthogonally polarized signals resulting either from hardware or from depolarization during propagation. The latter adds to thermal noise to decrease the effective SNR and must be accounted for when estimating the standard deviation of PDPP velocity estimates (see section 4 later on). With respect to phase noise, a random phase noise of 1° is assumed in the following simulation as a representative value of many currently available systems, while 0.1° and 10°

correspond to extremely good and mediocre values, respectively.

From the previous discussion two preliminary conclusions can be drawn. First, the steepness of the curves in the bottom panel of Fig. 3 at low T_{hv}s orients toward using T_{hv} values above 5 μs. Second, when targeting convective clouds, T_{hv} shorter than the extremely low coherency time values achievable in high turbulent media (60 μs) must be employed. This seems to constrain the range of possible useful values for T_{hv} into an interval that will be further narrowed by our analysis.

4. Notional studies of 3D convective scenarios

Here, forward simulations of realistic 3D convective profiles that account for several error sources associated with Doppler velocity estimates are presented.

a. Simulation framework

The radar signal is simulated by an end-to-end spaceborne Doppler radar simulator which couples a forward and a radar receiver model (Battaglia et al. 2011; Fig. 1). The forward model includes a Monte Carlo module (the Doppler Multiple Scattering simulator; Battaglia and Tanelli 2011) that accounts for multiple scattering, polarized radiation (necessary for simulating PD configurations) and interaction with a Kirchoff-type surface (Battaglia et al. 2008). The forward unit computes the cross and copolar reflectivities and the ideal (unfolded and noiseless) radar Doppler spectra as measured by a spaceborne radar flying over the 3D highly resolved scene under study. The contributions to the observed Doppler velocities from the satellite motion, the hydrometeor terminal velocity, and vertical air motion are properly coupled with the viewing geometry and the antenna pattern (Tanelli et al. 2002a). The forward model outputs the ideal radar Doppler spectrum at the H and V receiver channels using the contributions from the copolar (correlated) and cross-polar (uncorrelated) returns, S_V and S_H, at range r and flight time t:

$$S_H(r,t) = \overbrace{S_{hh}(r,t)}^{\text{corr.}} + \overbrace{S_{vh}(r-\Delta r,t)}^{\text{unc.}}, \tag{13}$$

$$S_V(r,t) = \underbrace{S_{vv}(r,t)}_{\text{correlated}} + \underbrace{S_{hv}(r+\Delta r,t)}_{\text{uncorrelated}}, \tag{14}$$

where the notation is the same as the one used in Eqs. (7) and (8). From the forward spectra, the radar receiver model derives the signal fluctuations measured at the radar antenna port [i.e., the I and Q (in phase and quadrature) time series] according to Kollias et al. (2013, manuscript submitted to *J. Atmos. Oceanic Technol.*) by including signal fluctuation due to the Markovian phase process and thermal noise (Zrnić 1975).

An important aspect in the simulation is to maintain the right correlations in the two I and Q time series for the different components of the H and V signals. The radar receiver model developed assuming that the radar range resolution is smaller than Δr follows the steps illustrated in Fig. 4:

(i) First, the $V_{corr} = I_{corr} + jQ_{corr}$ time series corresponding to the correlated spectrum [first term on the right-hand side of Eqs. (13) and (14)] are computed. The same random number sequence is used to transform spectra into an $I-Q$ time series (Zrnić 1975) to capture the fact that both components of that signal are generated by the same deterministic realization of the stochastic process represented by the ideal spectra. The number of $I-Q$ samples is obtained by dividing the integration time (during which the given spectrum is representative of the stationary process) by the pulse-pair distance T_{hv}. To account for random phase noise, a phase randomly in the interval $[-\tilde{\Phi} : +\tilde{\Phi}]$ is added to the I and Q phase. A value $\tilde{\Phi} = 1°$ is assumed (see previous discussion in section 3d).

(ii) Then, two I and Q time series corresponding to the uncorrelated components of the power signals are computed. Such components include both the second terms on the right-hand side of Eqs. (13) and (14) and the noise powers for each channel. Since all of them are not correlated, the two sequences for the H and V channels are generated with different seeds.

(iii) Correlated and uncorrelated I and Q sequences are summed up.

(iv) Finally, the I and Q time series (sampled at $1/T_{hv}$) are properly undersampled (red points versus blue points in Fig. 4) to simulate the sampling at frequency PRF (see Fig. 1).

b. Case study

The methodology previously described has been applied to two nadir-pointing configurations for the W and Ka bands with the same antenna size (see Table 1 for simulation parameters) for a variety of 3D convective scenes with 340-m horizontal resolution produced via Weather Research and Forecasting model simulations (Skamarock et al. 2007).

A case study of a spaceborne Doppler radar overpass over a convective core is considered here. The single scattering reflectivities and the mean Doppler velocity

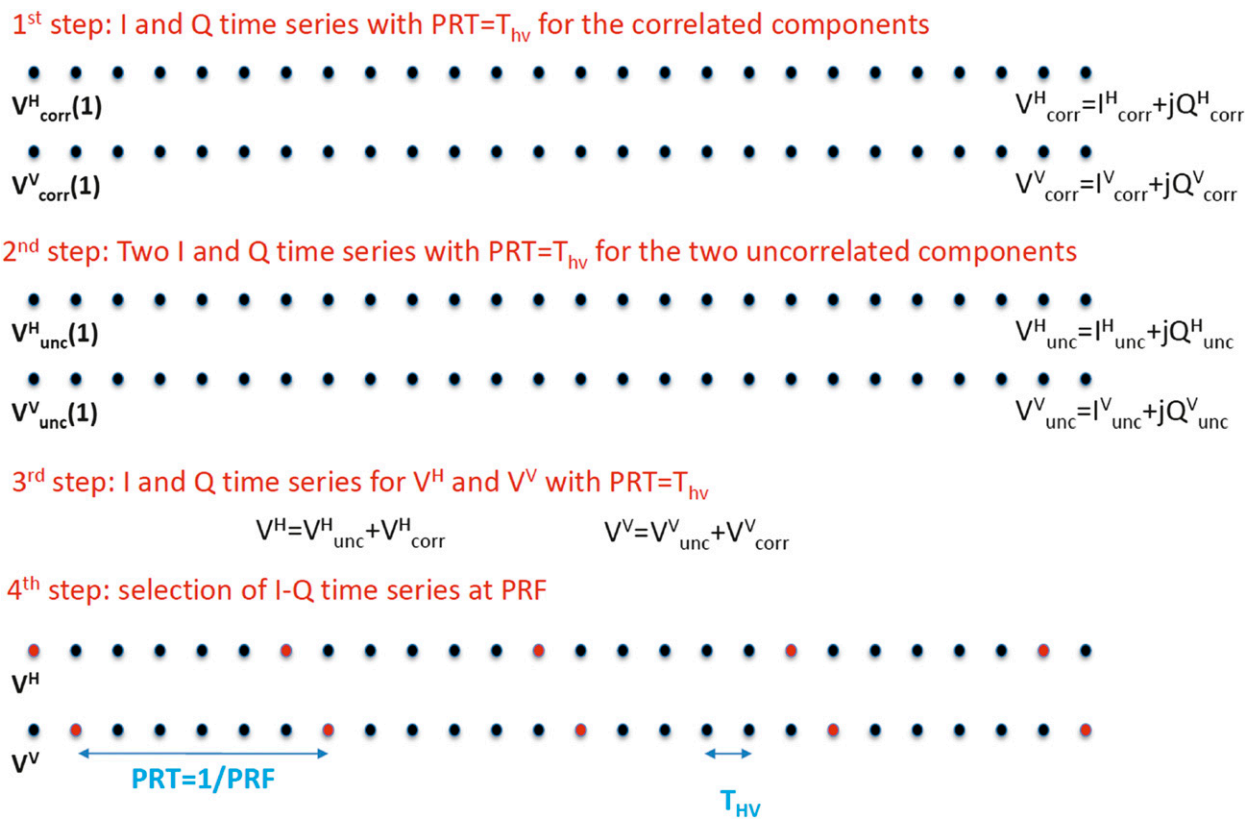

FIG. 4. Schematic for the simulation of the *I* and *Q* time series for a polarization diversity Doppler system.

for a platform with no satellite motion (top panels of Figs. 5, 6) epitomize two aspects. First, updrafts and downdrafts are contiguous both vertically, as in the development of thermals, and horizontally, as in the common presence of downdraft–updraft couplets, which generate strong vertical and horizontal shears of the vertical wind. Second, reflectivities and vertical velocities are not highly correlated: although large quantities of hydrometeors are often associated with updrafts, they are not exactly collocated with the updraft at scales that resolve a convective core. These features contribute to making dealiasing in convective clouds a highly challenging task especially if narrow Nyquist velocity boundaries are used, as is the case for the EarthCARE CPR. Experience gained from ground-based radar measurements from wind profilers suggests that Nyquist velocity values above 20 m s^{-1} are needed to dealias extreme convective scenarios with strong shears (Tridon et al. 2013). This Nyquist velocity value requires pulse-pair separations lower than 105 and 40 μs at the Ka and W bands, respectively.

The simulator outputs for radar reflectivities and Doppler velocities (inclusive of the effects from MS and satellite velocity) are shown in Figs. 5, 7 and in Figs. 6, 8 for the Ka and W bands, respectively. Comparison of the Ka- and W-band single scattering reflectivities (top left panels in Figs. 5, 6) clearly indicates deeper penetration from the top of the Ka-band radar in the convective core. The Ka signal has good SNR within the whole convective system; while the W band is strongly attenuated with Doppler profiling capabilities limited only to the upper part of the cloud (consider the red SNR contour lines). Single scattering Doppler velocities (top right panels in Figs. 5, 6) look quite similar, with differences mainly driven by the different spatial resolution (which favors more extreme velocities at the W band) and by Mie effects [which favor larger magnitude of velocities at the Ka band; Lhermitte (1990)].

The center left panels of Figs. 5, 6 show the noiseless forward model reflectivities (no radar receiver model involved); in regions with good SNR (i.e., >5 dB, red lines contours in the center panels) such reflectivities are neatly reproduced by the copolar MS reflectivities as obtained by the radar receiver model with noise (as detailed in the eighth column of Table 1) and PP processing at PRF = 7 kHz. Note that for our simulations $Z_{vv} = Z_{hh}$ since we are looking at azimuthally symmetric media at nadir. On the other hand, the forward model *V*

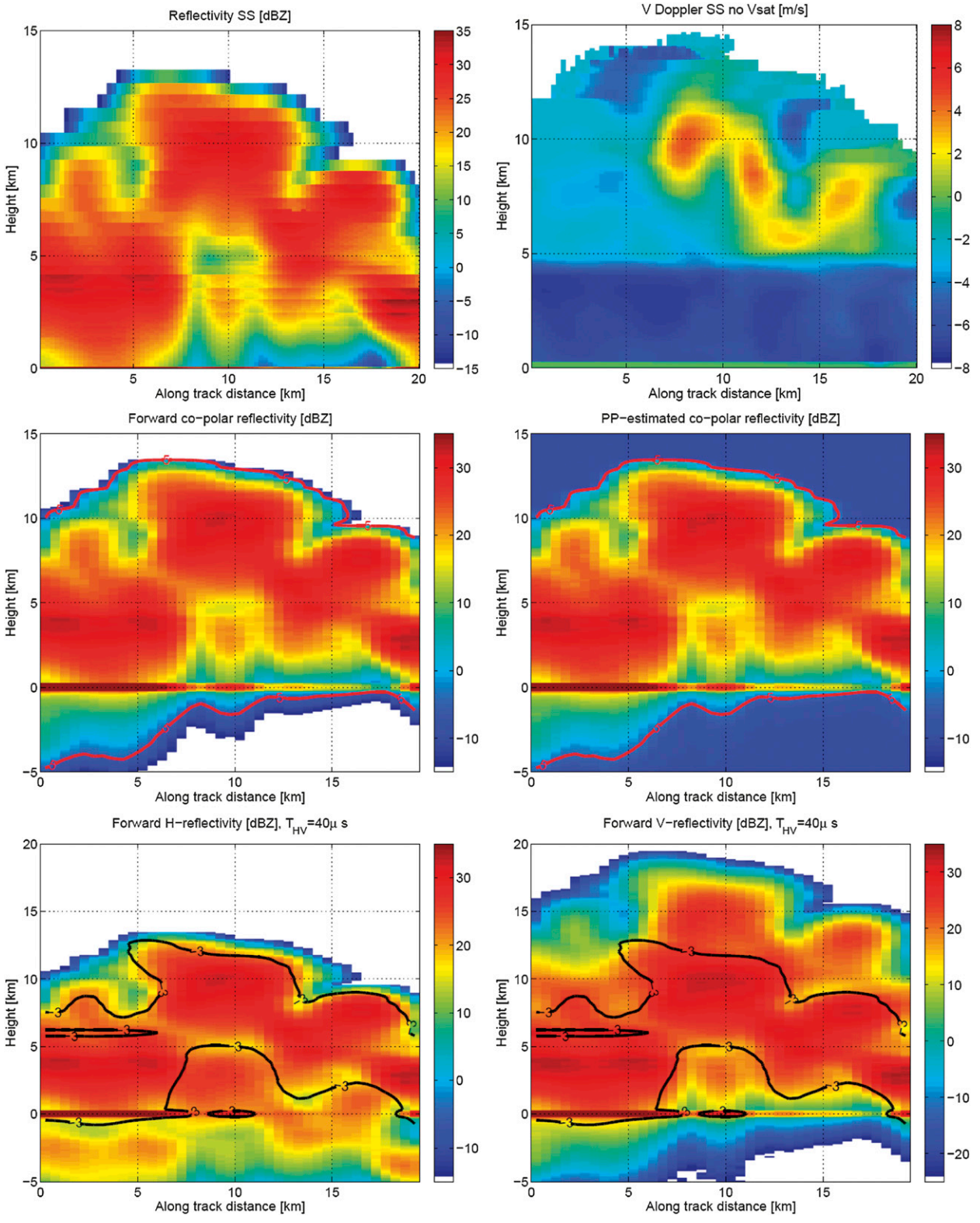

FIG. 5. Case study of a convective core at the Ka band. (top left) Single scattering reflectivity. (top right) Mean Doppler velocity for a platform with no satellite motion. (middle) (left) Forward and (right) PP-estimated copolar reflectivities. The red lines mark values where SNR = 5 dB. Forward (bottom) (left) Z^H and (right) Z^V reflectivity. The black contour lines enclose the region that is ghost free (i.e., where $\mathcal{G} < -3$ dB). The integration length is assumed to be 500 m.

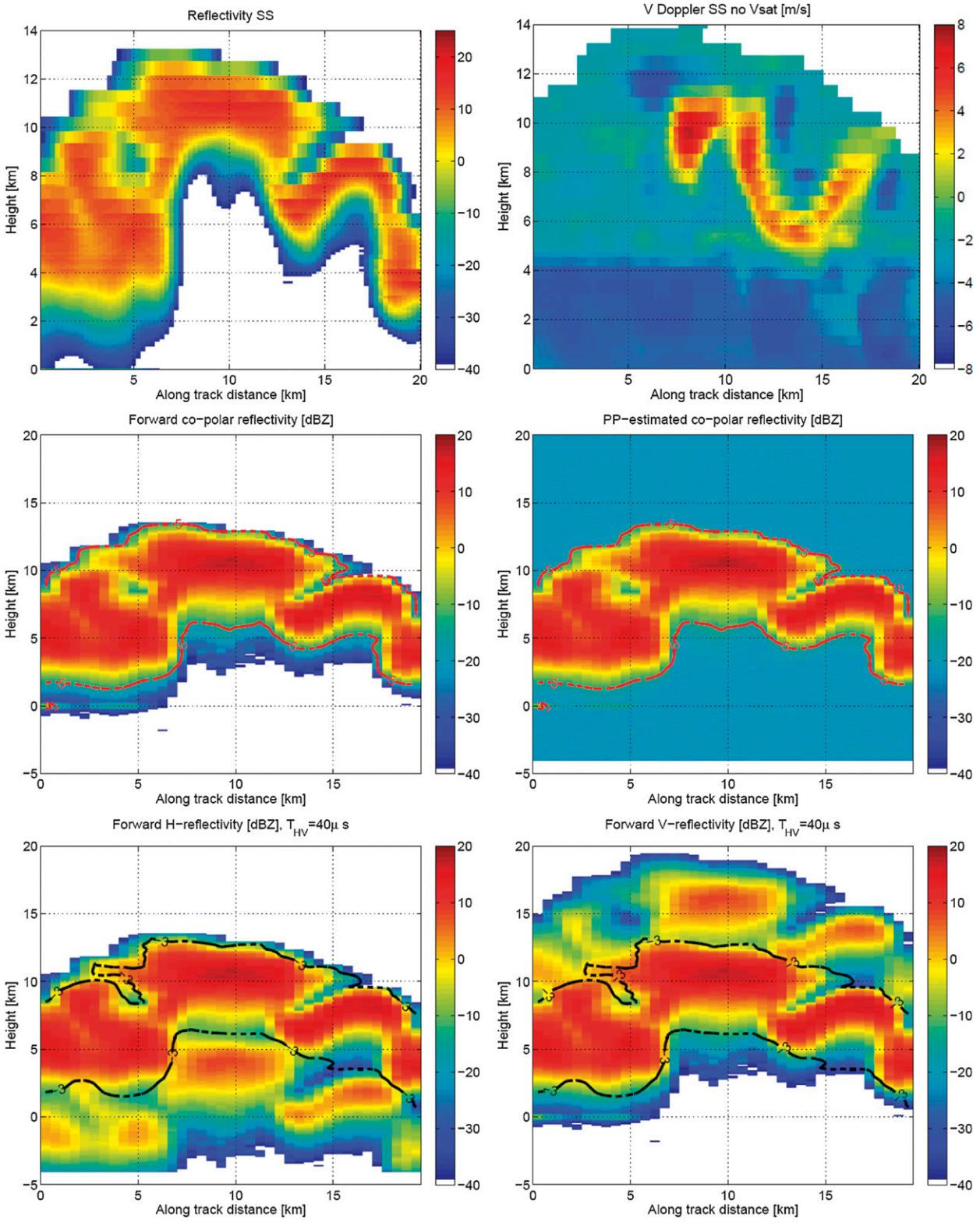

FIG. 6. Case study of a convective core. As in Fig. 5, but for the 94-GHz system.

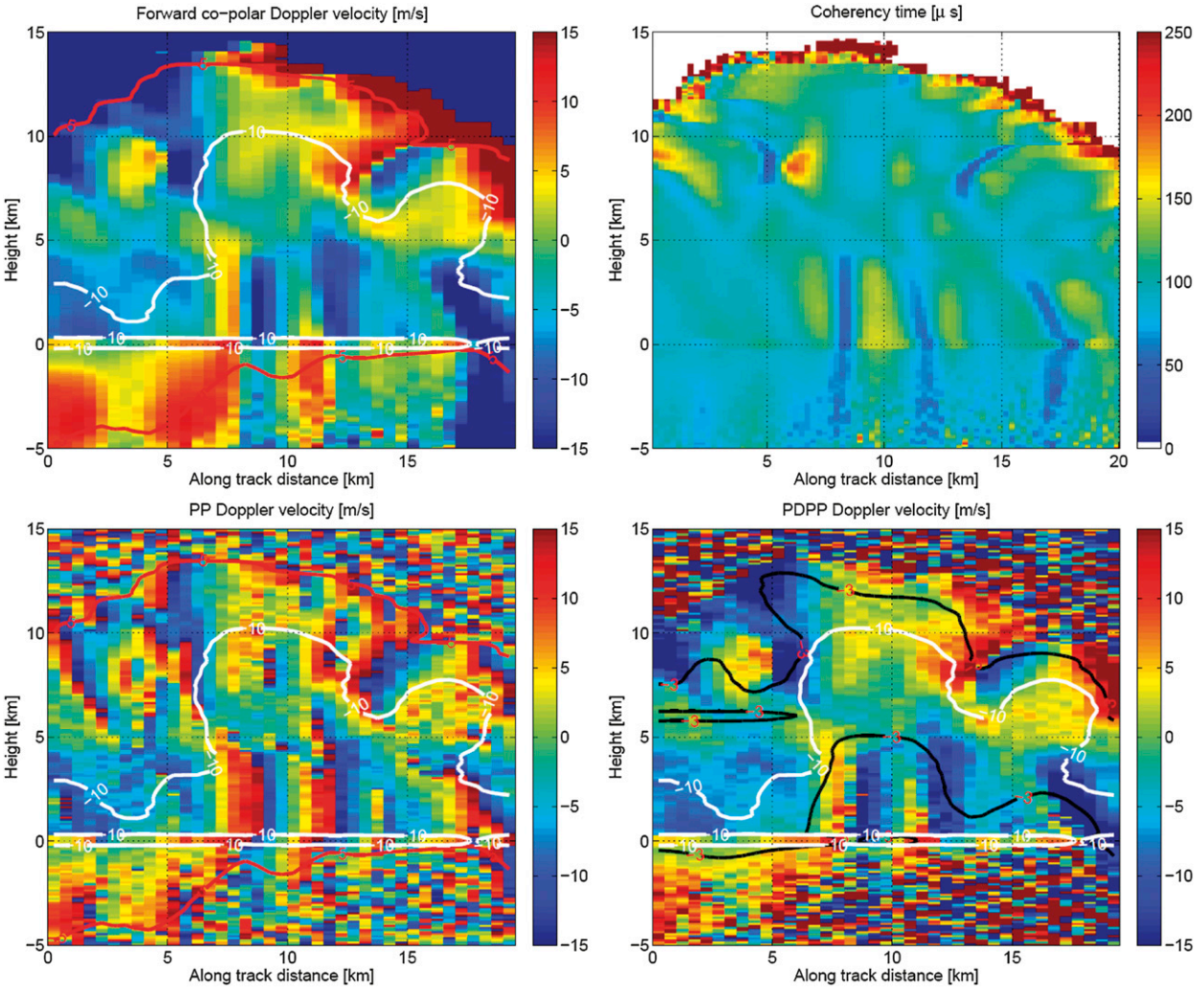

FIG. 7. Doppler velocity for a convective core at the Ka band. (top) (left) Forward Doppler velocity and (right) coherency time. (bottom) (left) PP-estimated and (right) PDPP-estimated Doppler velocity. The red, black, and white lines contour values where SNR = 5 dB, $\mathcal{G} = -3$ dB, and LDR $= -10$ dB, respectively. The PRF is 7 kHz while the integration length is equal to 500 m.

and H channel reflectivities (bottom panels in Figs. 5, 6) include the cross-talk terms [right term in the right hand side of Eqs. (13) and (14)], which in the simulation are generated by MS and by a ''background'' cross talk of -20 dB. Since the forward model only accounts for spherical particles, this value roughly accounts for the combination of atmospheric target depolarization (see discussion in section 3) and antenna cross isolation and it is used as a ballpark estimate. The effect of cross talk is to produce ghost returns in correspondence to a vertical shift equal ± 6 km ($T_{hv} = 40\,\mu$s) clearly visible at shorter and longer ranges for the H and V channels, respectively (cf. bottom panels with center left panels). At Ka the surface return is clearly visible for the whole length of the overpass and it represents a clear source of cross talk, at least for part of it (consider the black contour lines in the first 6 km).

The presence of strong attenuation, multiple scattering, and NUBF results in large discrepancies between the SS Doppler velocities estimated directly by the numerical model output, ignoring the sampling geometry and satellite motion (top right panels of Figs. 5, 6), and the simulated Doppler velocity (top left panels of Figs. 7, 8) even without the presence of noise and aliasing. However, it is obvious that because of the larger footprint the Ka band is strongly affected by NUBF effects that in regions of strong along-track reflectivity gradients, are driving the forward copolar Doppler velocities far away from the values ideally observed by a standing platform. This does certainly represent the biggest problem

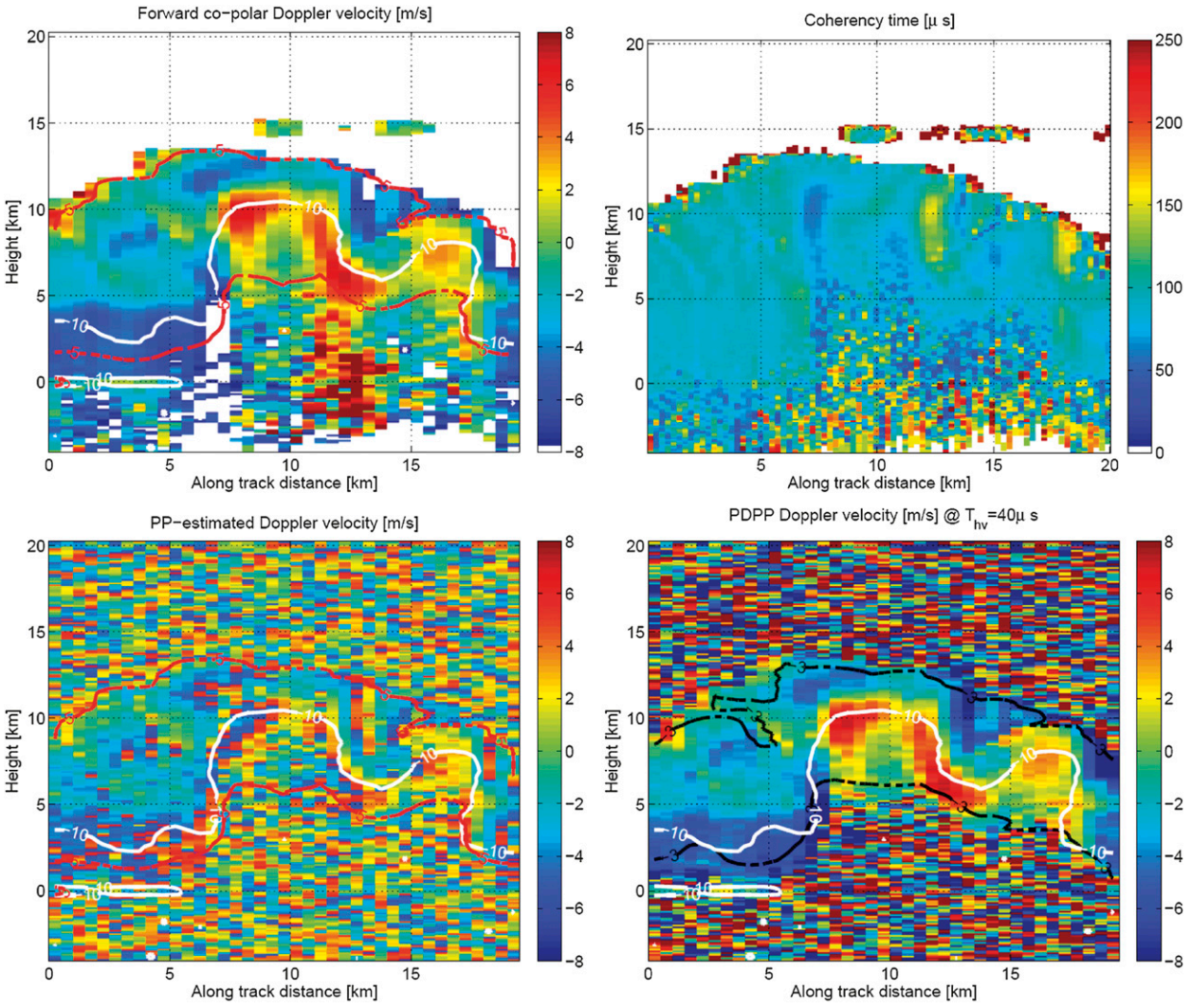

FIG. 8. Doppler velocity for a convective core. As in Fig. 7, but for 94 GHz.

and error source when considering observations of relatively small-scale convective features at footprint sizes comparable to the one assumed here for the Ka-band configuration (i.e., 2 km). On the other hand, except for regions close to cloud boundaries, the W-band signal follows the periodicity of updrafts and downdrafts because its footprint of 700 m is more adequate to resolve the fine features of this convective cell.

Assuming that ranges affected by MS can be adequately identified using LDR measurements (with LDR values lower than −10 dB sufficient to maintain the separation between MS and SS Doppler velocities below 1 m s^{-1}) and that NUBF-induced velocity biases can be removed using the along-track radar reflectivity gradient (Tanelli et al. 2002a; Sy et al. 2013), then we will use the forward copolar Doppler velocity (top left panel of Fig. 8) as our benchmark. The bottom panels in Figs. 7, 8 depict the mean Doppler velocity estimates for a standard pulse-pair system with pulse distance equal to 143 μs (i.e., PRF = 7 kHz) and a PDPP with T_{hv} = 40 μs and T_{int} = 1.43 ms (i.e., the single-polarization pulse is interlaced every nine PD pairs). A PRF value of 7 kHz is "border line" for an adequate unambiguous range window (21.4 km) but is used in this example to stretch the pulse-pair system potential to its very limit. As shown in top panel of Fig. 3, the PDPP technique does not suffer much by a reduction of the PRF, which is sometimes needed to properly profile the whole height of the storm (e.g., for tropical convective towers). While the PP estimates are strongly affected by aliasing problems, especially at the W band (blurred pixels in the bottom left panel of Fig. 8), caused by the low Nyquist (v_{Nyq} = 15 and 5.6 m s^{-1}), the PDPP technique (v_{Nyq} = 53.5 and 20 m s^{-1} for the specific T_{hv}) is capable of recovering the Doppler velocity field quite well. Note also

that the presence of the ghosts acts like a noise source with consequent deterioration of the Doppler accuracy (e.g., blurred pixels below 5 km for an along-track distance between 8 and 18 km at the W band). It is important to note that levels of MS contamination (consider the region below the white lines in Figs. 7, 8) are quite similar at the two different frequencies. This is due to the Ka larger footprint: in fact, as demonstrated in Battaglia et al. (2010) and Kobayashi et al. (2007), the amount of multiple scattering is proportional to the ratio between the footprint size and the mean free scattering length. In this case, the W-band shorter scattering length is compensated by a similar increase in footprint size at the Ka band (note that is not a general rule but true for this particular pair of configurations of frequencies and beamwidths). As a result the ghost-free region (consider the region between the black lines in Figs. 7, 8) is similar at the two wavelengths. Therefore, in this matched antenna configuration, the advantages in improved penetration offered by the Ka band with respect to the W band are only maintained in the region outside of the deep convective core. Inside the convective core instead the Doppler information is contaminated by MS at approximately the same altitude as in the W band, hence offering no additional view of the updraft–downdraft strength.

The profile corresponding to 7.75 km is shown in Fig. 9 for the two frequencies. The ghosts introduced by MS are clearly visible in the reflectivity profiles (top panels) at both frequencies. Where the reflectivity of such ghosts is significantly greater than the copolar reflectivity (e.g., heights above 13 and below 6.2 km at the W band), the Doppler velocity estimates based on the PDPP are very noisy (green lines erratically jumping within the Nyquist interval between $\pm 20\,\mathrm{m\,s^{-1}}$ at the W band). On the other hand, the PP technique (red line) is strongly affected by aliasing, with consequent problems in the identification of the downdraft in the upper part (e.g., at W-band heights above 11 km) and the updraft in the lower part (heights between 6 and 11 km). Conversely the PDPP estimates (green) match fairly well the expectation (blue) in the region between 2 and 12.5 km at Ka and between 6.5 and 13 km at W and with no aliasing at all and overall good accuracies. This figure illustrates the somewhat complementary nature of the limitations and advantages of the W- and Ka-band observations: on one hand, the Ka band does provide a few more kilometers of precise Doppler estimates inside the core; on the other hand, they are more affected by NUBF than the W band. While indeed overall the information in regards to the active part of the convection is visible in these simulated data, it is evident that accurate design of retrieval methods must include detection and correction of all these effects.

c. *Selection of optimal* T_{hv}

As discussed previously, the pulse-pair interval T_{hv} is a key parameter affecting:

(i) the Doppler velocity accuracy (see Fig. 3);
(ii) the shift of the uncorrelated ghosts (see Figs. 5, 6) and therefore areas where Doppler estimates become noisy; and
(iii) the Nyquist velocity v_{Nyq}.

The term T_{hv} has to be optimally selected in order to achieve good accuracy, to minimize aliasing, and to cover as much of the convective area as possible.

The simulation framework allows the determination of the regions that are ghost corrupted and assessment of the PDPP accuracy as a function of different T_{hv}s via computing the standard deviation and the bias of the pointwise error (relative to the forward model Doppler velocities) of the PDPP Doppler velocity estimates. The T_{hv} does not impact that portion of the profile that is affected by MS. It is therefore reasonable to compute such error only in regions marginally contaminated by MS. This is done by screening out regions severely affected by MS, where Doppler is completely meaningless (Battaglia and Tanelli 2011). Such regions can be easily identified either by the criterion discussed in Battaglia et al. (2011) or, if LDR measurements are available (e.g., if the interlaced configuration is adopted), by the condition $\mathrm{LDR} > -10\,\mathrm{dB}$ (A. Battaglia et al. 2013, unpublished manuscript). In portions of wet ice LDR can reach values around $-10\,\mathrm{dB}$, even in absence of MS; this would remove useful data, though it is well known that such regions are characterized by strong scattering and thus are likely to be affected by MS as well.

The use of an interlaced mode also allows the identification of the area contaminated by ghost signals. In fact, if we define a ghost over copolar signal ratio as

$$\mathcal{G}(r) \equiv 10\log_{10}\left\{\frac{Z_H(r) - Z_{\mathrm{hh}}(r) + Z_V(r) - Z_{\mathrm{vv}}(r)}{0.5[Z_{\mathrm{hh}}(r) + Z_{\mathrm{vv}}(r)]}\right\}, \tag{15}$$

[where Z_H, Z_V, Z_{hh}, and Z_{vv} are the reflectivities corresponding to the spectra S_H, S_V, S_{hh}, and S_{vv} defined in Eqs. (13) and (14), respectively] it is reasonable to assume that areas with $\mathcal{G} < -3\,\mathrm{dB}$ are "ghost free." The error analyses can then be restricted, in first instance, to the areas that are MS free (the onset of an MS-contaminated region is marked by the white lines in the bottom panels of Fig. 8) and, in second instance, to the areas that are simultaneously MS and ghost free (e.g., the region between the upper white and black lines in

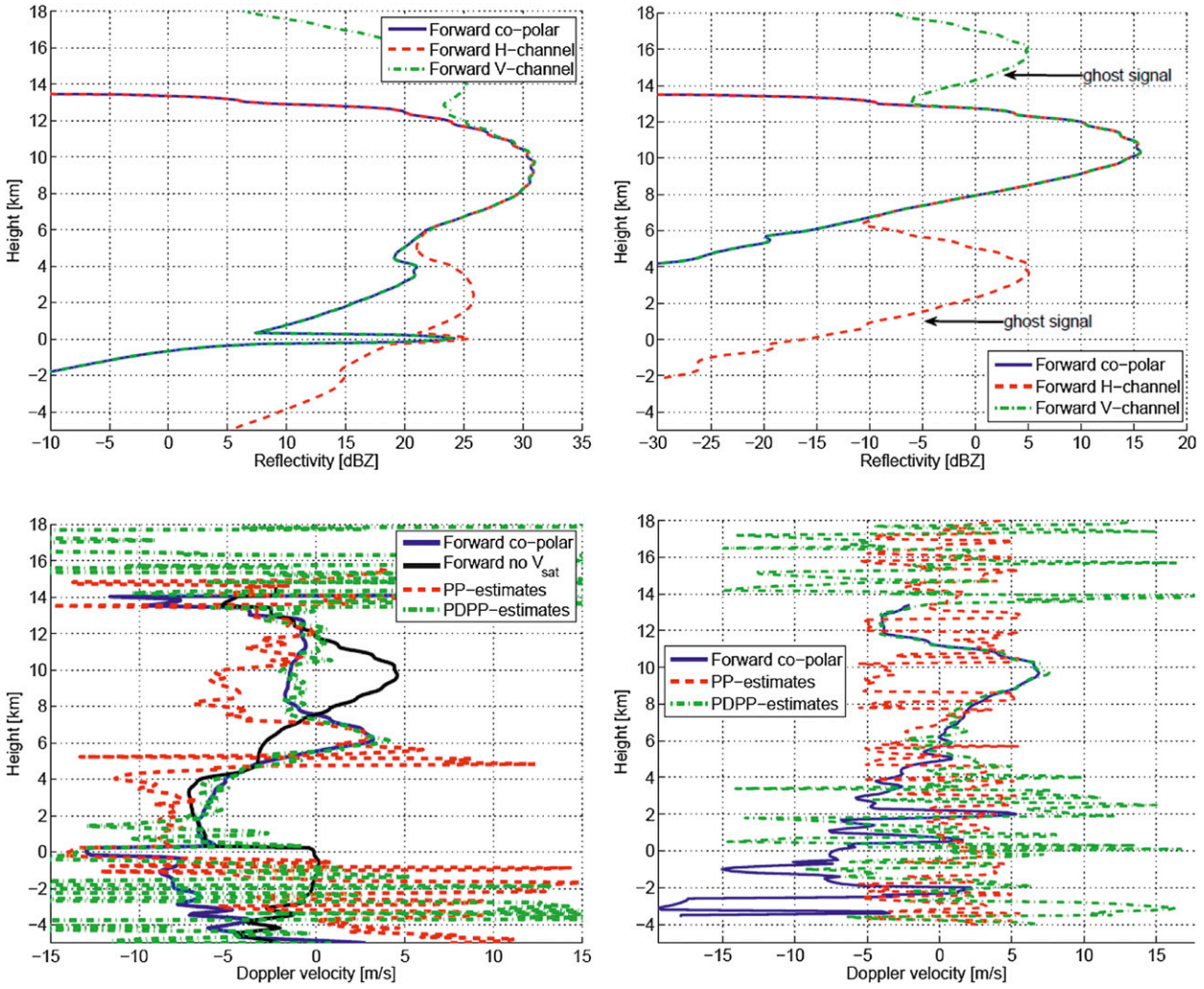

FIG. 9. (top) Reflectivity and (bottom) Doppler velocity profiles corresponding to the case depicted in Figs. 5 and 6 for the (left) Ka and (right) W bands for an along-track distance equal to 7.75 km.

the bottom left panels of Fig. 8). Figure 10 demonstrates that the PDPP technique provides a remarkable improvement for both frequencies compared to the standard PP technique, even in the ideal situation of perfect dealiasing (red lines versus green or blue lines). This confirms our previous considerations in section 3. Accuracy is significantly better at the W than at the Ka band by roughly a factor of 2 (cf. right and left panels), again in agreement with theoretical considerations. When selecting areas with SNR > 5 dB, accuracies below $0.7\,\mathrm{m\,s^{-1}}$ ($1.2\,\mathrm{m\,s^{-1}}$) can be achieved at the W (Ka) band in correspondence to T_{hv} values in the range between 15 and 50 μm (10 and 45 μm). However, this requires a proper identification of areas that are simultaneously MS and ghost free. The interlaced mode has the advantage of making such identification possible. Restricting the Doppler analysis to these regions has the clear benefit of improving the Doppler velocity accuracy at the price of further reducing the areas with Doppler estimates. This is demonstrated in the panels of Fig. 11, where the reduction in coverage is computed when different conditions are applied. As a reference, the value of detected pixels at SNR $= 0$ is assumed. For the ensemble of simulations here considered and for the single pulse noise level of Table 1, thanks to its better penetration depth, the Ka radar provides roughly 30% more coverage.

While the MS condition (blue lines) is T_{hv} independent, the ghost-free condition depends on the selection of T_{hv}. At large T_{hv}s ghost returns are widely spaced from copolar returns and the suppression of ghosts does not significantly reduce the number of pixels; vice versa, at small T_{hv}s the presence of ghost returns is minimized. Vice versa, intermediate values of T_{hv} between 10 and 40 μs

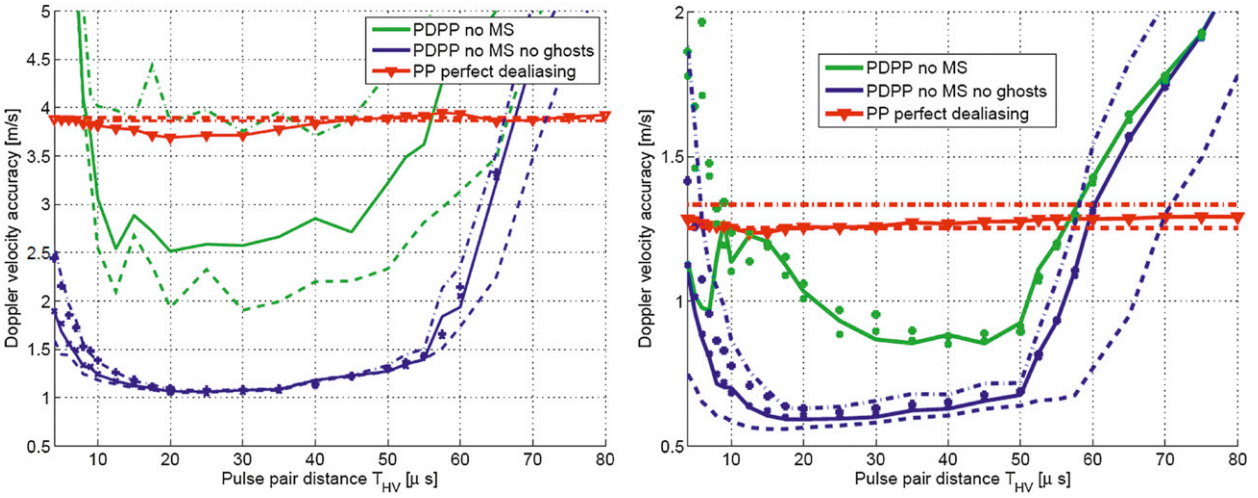

FIG. 10. Standard deviation of Doppler velocity errors for PP (with perfect dealiasing) and for PDPP technique for (left) Ka- and (right) W-band radar. Hundreds of convective profiles have been considered. A PRF = 7 kHz and an integration length of 500 m has been assumed. The dashed–dotted, continuous, and dashed lines correspond to regions with SNR > 0, 5, and 10 dB, respectively. A random phase noise of 1° has been assumed. The cross and plus curves correspond to a random phase noise of 0.1° and 10°, respectively.

(between 8 and 25 μs) at the Ka (W) band, respectively corresponding to a vertical shift of ± 1.5 and ± 6 km, maximize the overlapping effect, with a reduction of the useful area for Doppler down to less than 70%. This reasonably high percentage reflects the fact that for deep convective systems the blind layers introduced by the surface (Kobayashi et al. 2002) and by the large LDR returns of the melting layer are seldom a problem for the simple fact that surface returns are strongly (if not fully) attenuated by the above atmospheric column while the melting layer signature is simply not present. Both at the Ka and at the W bands the MS-free condition is substantially reducing the region for Doppler analysis by roughly 60% and 70%, respectively. Therefore, because of the larger footprint size, MS effects do play a crucial role at the Ka band as well. The 30% gain in coverage associated with the better penetration capabilities is partially lost because of MS contamination. Future studies should quantify the error introduced by MS as a function of the applied LDR threshold; this will allow

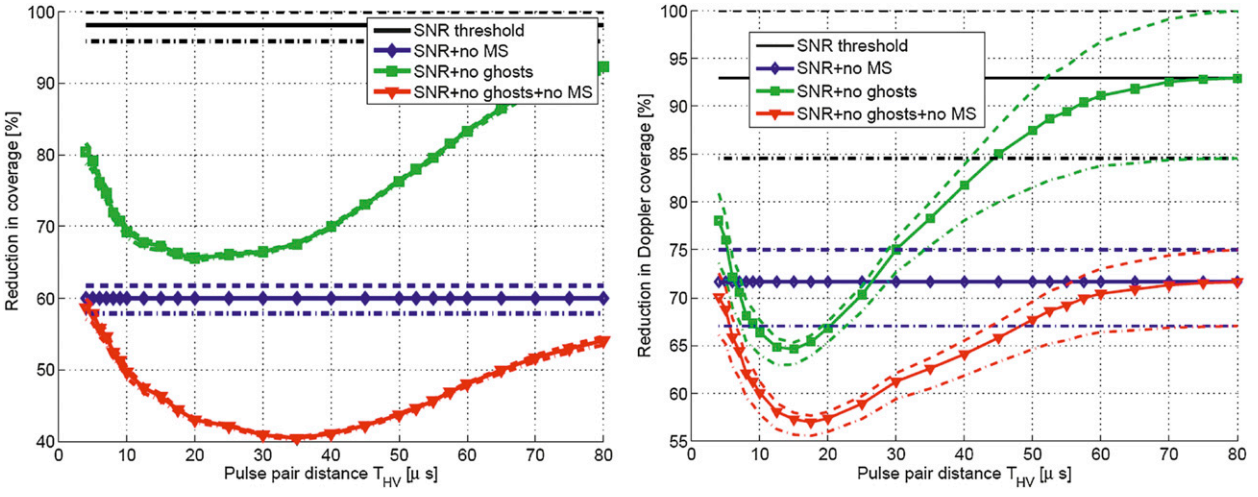

FIG. 11. Reduction in coverage as a function of T_{hv} when different conditions are applied to the simulation dataset profiles for (left) Ka- and (right) W-band radars. Different conditions are applied. 1) Black lines: SNR thresholding (with SNR = 0, 5, and 10 corresponding to dashed–dotted, continuous, and dashed lines). 2) Green lines: SNR thresholding plus ghost-free condition ($\mathcal{G} < -3$ dB). 3) Blue lines: SNR thresholding plus MS-free condition (LDR < -10 dB). 4) Red lines: SNR thresholding plus ghost-free condition plus MS-free condition. As a reference, the value of detected pixels at SNR = 0 is assumed.

a possibly lowering of our selected threshold of −10 dB in a way compatible with the science requirement when considering the overall velocity error budget.

When both the conditions on MS and ghosts are applied, the effect is obviously of a further reduction in Doppler area coverage. Again it is the Ka-band radar that is paying the higher price. For instance, a system employing $T_{hv} = 20\,\mu$s (which is the optimal choice from the accuracy point of view for both frequencies) is optimized when the coverage is reduced by a factor 0.45 and 0.57 (compared to the SNR = 0 dB detection level). This will almost perfectly compensate the advantage produced by the lower levels of attenuation at 35 GHz so that the Ka will provide basically the same useful coverage as the W-band system.

Finally, it is interesting to note that our results are not very sensitive to random phase noise. There is no appreciable difference between simulations performed with $\tilde{\Phi} = 0.1°$ and 1°, while only for T_{hv} smaller than 20 μs the Doppler accuracy with $\tilde{\Phi} = 10°$ is increasingly worse with decreasing T_{hv}s (cf. the blue plus symbol line with the continuous one in the top panels of Fig. 10). This is related to the fact that averaging over hundreds of pulses (corresponding to a 500-m along-track distance) is enough to cancel out the random phase noise, except at small T_{hv}s, where small phase errors are mapped into visible velocity errors.

5. Summary and conclusions

This study focuses on investigating the pros and cons of a PD configuration when employed on spaceborne millimeter radars observing deep convective cores. Such systems are particularly challenging for three reasons: 1) the extreme velocities produced inside such cores do require large Nyquist velocities (>20 m s^{-1}) to properly dealias the signal; 2) their vertical extent (with tropical convection reaching up to 20 km) precludes the use of large PRFs; and 3) the strong turbulence that tends to significantly broaden the Doppler spectra and reduce the radar coherency time. Though technologically more challenging and costly, polarization diversity offers a valid solution to overcome the classical range–Doppler dilemma, which, de facto, precludes the possibility of using millimeter spaceborne Doppler radars with antenna sizes of the order of 2.5 m for comprehensive convective studies. The very short decorrelation times that are characteristics of millimeter radar systems when observing deep convection (down to 50–60 μs) combined with the PRF upper limitation imposed by the depth of the troposphere makes the use of the single-polarization method impractical. Because of the weak coherence between successive pulses, staggered PRFs also become quite challenging with the likely occurrence of catastrophic errors (Torres et al. 2004).

The ambitious scientific requirement of 1 m s^{-1} accuracy at 500-m integration for reflectivities above −15 dBZ are within reach for a W-band radar with a 2.5-m antenna with optimal values of the pulse-pair interval between 20 and 30 μs but only once MS and ghost-contaminated regions are screened out. The PD technique is subject to cross-talk interference, phase noise, and thermal noise. All these effects are uncorrelated to the cloud signals; thus, they do not bias the estimated mean velocity but they do increase the standard deviation of the velocity estimate. Since MS produces LDR values exceeding −10 dB, MS effects are a primary source of cross talk in convective cores. It can be seriously detrimental for millimeter radar Doppler velocity accuracy, and it may appear, depending on T_{hv}, as ghost reflectivity signals in cloud-free areas. The identification of such areas is key for Doppler accuracies and can be achieved by employing an interlaced pulse-pair mode that measures the cross and the copolar reflectivities. The elimination of MS- and ghost-contaminated regions entails a reduction in coverage (respect to the SNR = 0 dB detection levels) of the order of 60%.

Because of its limited penetration in deep convection, a 94-GHz system with PD is ideal to characterize the upper part of convective cores only. A full characterization of the lower part requires a second lower frequency (Ku or Ka) as indeed is proposed in many concepts [e.g., for the ESA Earth Explorer 8 Polar Precipitation Missions (Joe et al. 2010), for the ESA–ISS Climate Dynamics Mission, and for the NASA Aerosol Cloud and Ecosystem mission (Durden et al. 2011)]. Our study demonstrates that though capable of fully penetrating most of the deep convective systems, a PD Ka radar with the same 2.5-m antenna size as the W-band radar enables useful Doppler information only in a region comparable to the one covered by the W-band system. This is because the increase in penetration is compensated by a larger reduction (<50%) in coverage caused by the elimination of MS- and ghost-contaminated regions. In addition, the larger footprint causes stronger NUBF effects—an additional source of uncertainties—while larger Nyquist velocities tend to reduce the Doppler accuracies. On the other hand, the larger Nyquist significantly reduces the impact of aliasing and facilitates both the aliasing correction and the NUBF correction with approaches as the one described in Sy et al. (2013). In summary, when focusing on deep convective cores, the addition of a Ka channel with matched antenna size to the W band resulting in a 2-km footprint provides only small advantages whose impact and usefulness should be carefully considered in light of the specific

scientific goals targeted. The obvious countermeasure is to increase the antenna size (at least in the along-track direction) as already proposed for the ACE mission Durden et al. (2011), with clear advantages both in terms of MS and NUBF effect reduction and of Doppler accuracy improvement (thanks to smaller Doppler spectral widths). In such a way the benefits of a PD configuration could be fully explored.

Our conclusions are applicable to deep convective observations using spaceborne Doppler radars. In convective scenarios the blind layers introduced by the surface and by the large LDR returns of the melting layer are rarely present. In particle sedimentation regimes (e.g., stratiform precipitation and cirrus clouds), due to the lack of strong dynamics and strong along-track reflectivity gradients, a PP technique performs well (Kollias et al. 2013, manuscript submitted to *J. Atmos. Oceanic Technol.*). The intuitive advantages in Doppler measurement of the Ka-band configuration that are downsized in this paper for deep convection remain mostly valid for scenarios such as shallow convection and cumulus congestus (where NUBF remains important, but MS is significantly reduced). Furthermore, while outside of the scope of this paper, one can gather from the simulations presented in this paper that also in deep convection the additional information provided by the profile of reflectivity at the Ka band significantly enhances our capability to characterize the microphysics of a large portion of a convective core. A complete characterization of the error budget of millimeter spaceborne Doppler radars in deep convection, which accounts for NUBF, multiple scattering, mispointing, aliasing, and Doppler moment estimate errors is part of ongoing research. This study demonstrates that PD represents a very promising methodology capable of significantly reducing the last two sources of error, a key step to achieving typical mission requirements for convection-oriented millimeter radar-based spaceborne missions.

Acknowledgments. The portion of work carried out by Battaglia and Kollias was supported by the European Space Agency under the WISDR (capability of atmospheric parameter retrieval and modeling for Wide-Swath Spaceborne Doppler Radars) activity (ITT AO/1-6661/11/NL/LvH) and by CEOI under the POLYDOROS (POLARIZATION Diversity Doppler Radar on Satellite) project. A portion of this work (Tanelli) was carried out in support to the ACE mission concept and to cloud and precipitation science at the Jet Propulsion Laboratory, California Institute of Technology, under a contract with the National Aeronautics and Space Administration.

REFERENCES

Allan, R. P., and B. J. Soden, 2008: Atmospheric warming and the amplification of precipitation extremes. *Science,* **321,** 1481–1484, doi:10.1126/science.1160787.

Amayenc, P., J. Testud, and M. Marzoug, 1993: Proposal for a spaceborne dual-beam rain radar with Doppler capability. *J. Atmos. Oceanic Technol.,* **10,** 262–276.

Bacmeister, J. T., and G. L. Stephens, 2011: Spatial statistics of likely convective clouds in *CloudSat* data. *J. Geophys. Res.,* **116,** D04104, doi:10.1029/2010JD014444.

Battaglia, A., and S. Tanelli, 2011: DOMUS: Doppler Multiple Scattering Simulator. *IEEE Trans. Geosci. Remote Sens.,* **49,** 442–450, doi:10.1109/TGRS.2010.2052818.

——, M. O. Ajewole, and C. Simmer, 2007: Evaluation of radar multiple scattering effects in *CloudSat* configuration. *Atmos. Chem. Phys.,* **7,** 1719–1730.

——, S. Kobayashi, S. Tanelli, E. Im, and C. Simmer, 2008: Multiple scattering effects in pulsed radar systems: An intercomparison study. *J. Atmos. Oceanic Technol.,* **25,** 1556–1567.

——, S. Tanelli, S. Kobayashi, D. Zrnić, R. Hogan, and C. Simmer, 2010: Multiple-scattering in radar systems: A review. *J. Quant. Spectrosc. Radiat. Transfer,* **111,** 917–947, doi:10.1016/j.jqsrt.2009.11.024.

——, T. Augustynek, S. Tanelli, and P. Kollias, 2011: Multiple scattering identification in spaceborne W-band radar measurements of deep convective cores. *J. Geophys. Res.,* **116,** D19201, doi:10.1029/2011JD016142.

Bennartz, R., P. Joe, U. Loehnert, J. Koskinen, G. Skofronick-Jackson, and D. Vane, Eds., 2011: Report on the third international workshop on space-based snowfall measurement. 30 pp. [Available online at http://www.isac.cnr.it/~ipwg/meetings/grainau-2011/iwssm_3_report_final.pdf.]

Doviak, R. J., and D. Sirmans, 1973: Doppler radar with polarization diversity. *J. Atmos. Sci.,* **30,** 737–738.

——, and D. S. Zrnić, 1984: *Doppler Radar and Weather Observations.* Academic Press, 458 pp.

Durden, S. L., and Coauthors, 2011: A cloud and precipitation radar system concept for the ACE Mission. JPL Tech. Rep., 4 pp. [Available online at http://trs-new.jpl.nasa.gov/dspace/bitstream/2014/42129/1/11-1720.pdf.]

Heymsfield, G. M., L. Tian, A. J. Heymsfield, L. Li, and S. Guimond, 2010: Characteristics of deep tropical and subtropical convection from nadir-viewing high-altitude airborne Doppler radar. *J. Atmos. Sci.,* **67,** 285–308.

Hu, Y.-X., D. Winker, P. Yang, B. Baum, L. Poole, and L. Vann, 2001: Identification of cloud phase from PICASSO-CENA lidar depolarization: a multiple scattering sensitivity study. *J. Quant. Spectrosc. Radiat. Transfer,* **70,** 569–579.

Joe, P., and Coauthors, 2010: The polar precipitation measurement mission. *Proc. Sixth European Conf. on Radar Meteorology and Hydrology: Satellite Radar Measurements and Hydro-Meteorological Applications,* Sibiu, Romania, ERAD, 18 pp. [Available online at http://www.erad2010.org/pdf/oral/tuesday/satellite/01_ERAD2010_Joe.pdf.]

Kobayashi, S., H. Kumagai, and H. Kuroiwa, 2002: A proposal of pulse-pair Doppler operation on a spaceborne cloud-profiling radar in the W band. *J. Atmos. Oceanic Technol.,* **19,** 1294–1306.

——, ——, and T. Iguchi, 2003: Accuracy evaluation of Doppler velocity on a spaceborne weather radar through a random signal simulation. *J. Atmos. Oceanic Technol.,* **20,** 944–949.

——, T. Oguchi, S. Tanelli, and E. Im, 2007: Backscattering enhancement on spheroid-shaped hydrometeors: Considerations

in water and ice particles of uniform size and Marshall-Palmer distributed rains. *Radio Sci.,* **42,** RS2001, doi:10.1029/2006RS003503.

Lhermitte, R., 1990: Attenuation and scattering of millimeter wavelength radiation by clouds and precipitation. *J. Atmos. Oceanic Technol.,* **7,** 464–479.

Liao, L., R. Meneghini, and T. Iguchi, 1999: Simulations of mirror image returns of air/space-borne radars in rain and their applications in estimating path attenuation. *IEEE Trans. Geosci. Remote Sens.,* **37,** 1107–1121.

Luo, G. Y., and G. L. Stephens, 2010: Use of A-Train data to estimate convective buoyancy and entrainment rate. *Geophys. Res. Lett.,* **37,** L09804, doi:10.1029/2010GL042904.

Luo, Z., G. Y. Liu, and G. L. Stephens, 2008: *CloudSat* adding new insight into tropical penetrating convection. *Geophys. Res. Lett.,* **35,** L19819, doi:10.1029/2008GL035330.

National Research Council of the National Academies, 2007: *Earth Science and Applications from Space: National Imperatives for the Next Decade and Beyond.* National Academies Press, 456 pp.

Parazoo, N. C., A. S. Denning, J. A. Berry, A. Wolf, D. A. Randall, S. R. Kawa, O. Pauluis, and S. C. Doney, 2011: Moist synoptic transport of CO_2 along the mid-latitude storm track. *Geophys. Res. Lett.,* **38,** L09804, doi:10.1029/2011GL047238.

Pazmany, A., J. Galloway, J. Mead, I. Popstefanija, R. McIntosh, and H. Bluestein, 1999: Polarization diversity pulse-pair technique for millimeter-wave Doppler radar measurements of severe storm features. *J. Atmos. Oceanic Technol.,* **16,** 1900–1910.

Phillips, V. T. J., and L. J. Donner, 2006: Cloud microphysics, radiation and vertical velocities in two- and three-dimensional simulations of deep convection. *Quart. J. Roy. Meteor. Soc.,* **132,** 3011–3033, doi:10.1256/qj.05.171.

Sachidananda, M., and D. Zrnić, 2002: An improved clutter filtering and spectral moment estimation algorithm for staggered PRT sequences. *J. Atmos. Oceanic Technol.,* **19,** 2009–2019.

Schutgens, N. A. J., 2008: Simulated Doppler radar observations of inhomogeneous clouds: Application to the EarthCARE space mission. *J. Atmos. Oceanic Technol.,* **25,** 1514–1528.

Skamarock, W. C., J. B. Klemp, J. Dudhia, D. O. Gill, D. M. Barker, W. Wang, and J. G. Powers, 2007: A description of the Advanced Research WRF version 2. NCAR Tech. Note NCAR/TN-468+STR, 88 pp.

Stephens, G. L., and Coauthors, 2010: Dreary state of precipitation in global models. *J. Geophys. Res.,* **115,** D24211, doi:10.1029/2010JD014532.

Sy, O., S. Tanelli, N. Takahashi, Y. Ohno, H. Horie, and P. Kollias, 2013: Simulation of EarthCARE spaceborne Doppler radar products using ground-based and airborne data: Effects of aliasing and nonuniform beam-filling. *IEEE Trans. Geosci. Remote Sens.,* doi:10.1109/TGRS.2013.2251639, in press.

Tanelli, S., E. Im, S. L. Durden, L. Facheris, and D. Giuli, 2002a: The effects of nonuniform beam filling on vertical rainfall velocity measurements with a spaceborne Doppler radar. *J. Atmos. Oceanic Technol.,* **19,** 1019–1034.

——, ——, L. Facheris, and E. A. Smith, 2002b: DFT-based spectral moment estimators for spaceborne Doppler precipitation radar. *Proc. Symp. on Remote Sensing of the Atmosphere, Environment and Space,* 4894, Hangzhou, China, SPIE, doi:10.1117/12.467754.

——, ——, L. F. Stephen, and L. Durden, 2003: Measuring vertical rainfall velocity through spaceborne Doppler radar: Performance analysis and system requirements. *IGARSS '03: Int. Geoscience and Remote Sensing Symp.,* Toulouse, France, IEEE, 878–880.

——, S. Durden, E. Im, K. Pak, D. Reinke, P. Partain, J. Haynes, and R. Marchand, 2008a: *CloudSat*'s cloud profiling radar after 2 years in orbit: Performance, calibration, and processing. *IEEE Trans. Geosci. Remote Sens.,* **46,** 3560–3573.

——, E. Im, S. Durden, D. Giuli, and L. Facheris, 2008b: Spaceborne Doppler radars for atmospheric dynamics and energy budget studies. *Radar Conf.,* Rome, Italy, IEEE, 1–6, doi:10.1109/RADAR.2008.4721127.

——, S. L. Durden, E. Im, G. Heymsfield, P. Racette, and D. Starr, 2009: Next-generation spaceborne cloud profiling radars. *Radar Conf.,* Pasadena, CA, IEEE, 1–4, doi:10.1109/RADAR.2009.4977116.

Torres, S. M., Y. F. Dubel, and D. S. Zrnić, 2004: Design, implementation, and demonstration of a staggered PRT algorithm for the WSR-88D. *J. Atmos. Oceanic Technol.,* **21,** 1389–1399.

Trenberth, K. E., A. Dai, R. M. Rasmussen, and D. B. Parsons, 2003: The changing character of precipitation. *Bull. Amer. Meteor. Soc.,* **84,** 1205–1217.

Tridon, F., A. Battaglia, and P. Kollias, 2013: Signal postprocessing and reflectivity calibration of the Atmospheric Radiation Measurement program 915-MHz wind profilers. *J. Atmos. Oceanic Technol.,* **30,** 1038–1054.

Ulaby, F. T., R. K. Moore, and A. K. Fung, 1986: *Microwave Remote Sensing Active and Passive.* Artech House, 608 pp.

van den Heever, S., and W. Cotton, 2004: The impact of hail size on simulated supercell storms. *J. Atmos. Sci.,* **61,** 1596–1609.

Wolde, M., and G. Vali, 2001: Polarimetric signatures from ice crystals observed at 95 GHz in winter clouds. Part I: Dependence on crystal form. *J. Atmos. Sci.,* **58,** 828–841.

Yano, J.-I., E. Machulskaya, P. Bechtold, and R. S. Plant, 2013: Bells and whistles of convection parameterization. *Bull. Amer. Meteor. Soc.,* **94,** ES5–ES7.

Zhang, G. J., and X. Song, 2009: Interaction of deep and shallow convection is key to Madden-Julian oscillation simulation. *Geophys. Res. Lett.,* **36,** L09708, doi:10.1029/2009GL037340.

Zrnić, D. S., 1975: Simulation of weatherlike Doppler spectra and signal. *J. Appl. Meteor.,* **14,** 619–620.

——, 1977: Spectral moment estimates from correlated pulse pairs. *IEEE Trans. Aerosp. Electron. Syst.,* **AES-13,** 344–354.

——, 1979: Estimation of spectral moments for weather echoes. *IEEE Trans. Geosci. Electron.,* **GE-17,** 113–128.